Exploring the effect of the pH on the corrosion of multilayer nickel-chromium coatings

Vega, Jesús Manuel; Ganborena, Larraitz; Gonzalez-Garcia, Yaiza; Özkaya, Berkem; Grande, Hans Jürgen; García-Lecina, Eva

DOI
10.1016/j.corsci.2022.110819

Publication date
2023

Document Version
Final published version

Published in
Corrosion Science

Corrosion Science 210 (2023) 110819

Contents lists available at ScienceDirect

Corrosion Science

journal homepage: www.elsevier.com/locate/corsci

Exploring the effect of the pH on the corrosion of multilayer nickel-chromium coatings

Jesús Manuel Vega [a,*], Larraitz Ganborena [a], Yaiza Gonzalez-Garcia [b], Berkem Özkaya [c], Hans-Jürgen Grande [a,d], Eva García-Lecina [a]

[a] CIDETEC, Basque Research and Technology Alliance (BRTA), Paseo Miramón 196, 20014 Donostia-San Sebastián, Spain
[b] Delft University of Technology, Department of Materials Science and Engineering, Mekelweg 2, 2628 CD Delft, the Netherlands
[c] Atotech Deutschland GmbH, Postfach 21 07 80, 10507 Berlin, Germany
[d] University of the Basque Country (UPV/EHU), Advanced Polymers and Materials: Physics, Chemistry and Technology Department, Avda. Tolosa 72, 20018 Donostia San Sebastian, Spain

ARTICLE INFO

Keywords:
Metal coatings
Acidic solutions
Polarisation
SEM
Electrodeposited films
Oxygen reduction

ABSTRACT

The impact of the pH on the corrosion of microporous nickel-chromium coatings has been explored at localised scale by Scanning Electrochemical Microscopy and validated by potentiodynamic polarisation measurements. Results not only reveal the correlation between both techniques but also enables to identify the different corrosion rate after increasing the electrolyte aggressiveness varying the pH. However, independently of the pH, a similar corrosion mechanism was determined: the cross-section micrographs (by Field Emission-Scanning Electron Microscope) have revealed an isotropic growth of the actives sites at early-stage corrosion as well as the attack of different nickel layers during the corrosion propagation.

1. Introduction

In general, corrosion resistance is a prerequisite for functional coatings exposed to aggressive environments in order to ensure their proper operation. On the other hand, there are also coatings devoted to decorative applications [1–4] which not only have to maintain its attractive appearance during aging but also have to provide enhanced corrosion resistance capabilities. This requirement is imposed on decorative nickel-chromium multilayer coatings for outdoor applications (e.g. automotive industry) [5]. Usually, these types of coatings posse a multilayer configuration based on a polymeric substrate (not exclusively) having an electroless deposited copper layer followed by several nickel layers and finally, a plated chromium layer on the top. In general, one or two types of nickel layers have been used in the past [6–8]. However, to provide enhanced corrosion performance at least three layers are needed [9–11]. Therefore, the most common configuration for outdoor applications is based on: a thin topmost microporous plated chromium layer (usually around 250 nm thickness [12]) and three underneath nickel layers consisting of a microporous layer (MP Ni), an intermediate bright nickel layer (B Ni) and a semi-bright (SMB Ni) one at the bottom.

In our previous works [9–11], the corrosion behaviour of these systems (3 nickel layers) has been studied during exposure to acidified chloride-based electrolyte containing cupric ions (aggressive environment used on copper-accelerated acetic acid-salt spray (CASS) test [13]). All nickel layers have a different corrosion potential with the bright nickel being the layer with less noble potential [10]. Such a design aims to preserve the aesthetic of the chromium layer (acting as cathode thanks to the passive oxide layer [12]), guiding the corrosion front toward the intermediate nickel layer which is acting as anode. Since this layer is located between the other two nickel ones with more noble potential, it is ensured that the corrosion only occurs in there, maintaining the pristine appearance of the topmost chromium layer [14–16]. In general, either micro-pores or micro-cracks are intended to decrease the ratio cathodic (top-chromium layer): anodic (nickels underneath) area. In this way, a homogenous current distribution is provided by the defects which are acting as localised spots for the initiation of the galvanic corrosion all around the surface [15]. However, the above-mentioned corrosion mechanism seems to only be maintained when cupric ions are present in the electrolyte as was observed by Ganborena et al. [10]. This work indicated that the design of the multilayer configuration fails in absence of a strong oxidant (e.g., cupric

* Corresponding author.
E-mail address: jvega@cidetec.es (J.M. Vega).

https://doi.org/10.1016/j.corsci.2022.110819
Received 29 July 2022; Received in revised form 4 October 2022; Accepted 7 November 2022
Available online 8 November 2022

ions) due to the galvanic coupling between nickel layers is not preserved. The morphology and propagation of the corrosion attack with time in a chloride-based electrolyte are not yet fully understood. In fact, from the industrial point of view, only the aesthetic damage of the topmost surface is evaluated after specific periods of exposure to the CASS test [13]. Limited investigations have been done focusing on the early-stages of the corrosion and corrosion propagation inside the nickel layers with time. In addition, little attention has been given to the impact of the pH without cupric ions (i.e., non-acidified/acidified electrolyte at pH = 3.1) on the corrosion mechanism of these multi-layer systems.

The corrosion phenomena at localised scale cannot be neglected for these systems due to the presence of micro-discontinuities. Conventional electrochemical methods such as potentiodynamic polarisation and electrochemical impedance spectroscopy (EIS) cannot provide information on the processes taking place on the surface with localised (or spatial) resolution. Under this scenario, localised techniques can overcome this limitation. As an example, Scanning Vibrating Electrode Technique (SVET) is able to provide information at localised scale about the impact of Cu in the microstructure and corrosion behaviour of Ni-based coatings [17]. Regarding this type of coatings, Scanning Kelvin Probe (SKP) was able to reveal localised cathodes for this system [9], and different operation modes of the Scanning Electrochemical Microscope (SECM) have been used to study galvanic corrosion phenomena (e.g., potentiometric SECM, dual microelectrode to simultaneously detect metallic cations and pH, etc.) [18–23]. In our previous work [11], the versatility of the SECM technique to identify the different corrosion reactions taking place on multi-layer nickel-chromium coatings was demonstrated while immersed in CASS electrolyte (i.e., acidic pH 3.1 chloride-based solution containing cupric ions). Two SECM operation modes, redox competition and surface generation/tip collection were employed to reveal the role of the cupric ions on the corrosion mechanism of the multi-layer coatings. Therefore, SECM is a powerful method to investigate electrochemical (corrosion) activities with high spatial resolution [24]. However, as mentioned above, the corrosion mechanism differs in the absence of cupric ions, and the local activity (cathodic reactions) in chloride-based electrolytes without cupric ions has not been explored yet for these coatings. Moreover, a dynamic corrosion process lasting for days needs to be studied in detail at localised scale.

This work aims to provide new insights about the corrosion mechanism (at early-stage and during the corrosion propagation) of microporous nickel-chromium coatings in chloride-based electrolytes as a function of the pH. Two chloride-based electrolytes have been used: a non-acidified and the acidified one (at pH 3.1). SECM experiments operating in competition mode were carried out to monitor the evolution with time of the possible cathodic reactions during the corrosion process. Additionally, potentiodynamic polarisation curves and the FE-SEM micrographs were obtained to validate the SECM observations and to postulate the corrosion mechanism of the multi-layer nickel-chromium coatings in chloride-based solution.

2. Experimental details

2.1. Materials

Microporous nickel-chromium multilayer coatings were obtained from trivalent chromium baths following the procedure described elsewhere [10], using acrylonitrile butadiene styrene (ABS) as the substrate with an intermediate copper layer able to promote the adhesion with bottommost nickel layer.

The thickness of the Cr layer was measured by using the Fischerscope XDV-SDD Energy Dispersive X-ray Fluorescence spectrometer (XRF). The thickness of each nickel layer and the relative potential difference between them was determined by Simultaneous Thickness and Electrochemical Potential (STEP) test according to ASTMB764. Before testing, samples were cleaned with acetone, rinsed with deionized water and dried with a compressed air gun.

A schematic representation of the multilayer system is shown in Fig. 1(a). The complete multilayer system was formed from top to bottom with the following metallic layers: i) microporous chromium (200 ± 20 nm), ii) microporous nickel (MPS Ni, 1.4 ± 0.2 μm), iii) bright nickel (B Ni, 10.7 ± 1.4 μm), and iv) semibright nickel (SB Ni, 12.2 ± 1.7 μm). The following potential difference was found: 103 ± 11 mV between MPS/B Ni layers and 189 ± 23 mV between SB/B Ni layers. This difference was achieved having Ni layers with different concentration of S (i.e., B Ni layer has the largest content of S).

Two different electrolytes have been used, varying the pH: i) 5% wt. NaCl at the natural pH of the solution (labelled as "Cl_N^- electrolyte") and ii) 5% wt. NaCl adjusted at pH 3.1 (labelled as "Cl_H^- electrolyte"). All solutions were prepared with analytical grade reagent and 18.5 MΩcm deionised water and the resistivity was around 45 Ω·cm at 25ºC. The solution pH was adjusted with the addition of Glacial acetic acid.

2.2. Surface and cross-section characterisation

Field emission scanning electron microscope (FE-SEM) Gemini Ultraplus from Zeiss was employed to characterise the samples. Fig. 1(b) shows a micrograph with the typical morphology of the surface, having a micropore as discontinuity created by an Al_2O_3 particle. Cross-section of the samples after different exposure times (from 3.5 h to 92 h) to the different electrolytes (under OCP). Samples were cut and embedded in an epoxy cold mounting resin. Metallographic preparation was performed using SiC papers up to FEPA P4000 grit, followed by polishing with polycrystalline diamond water-based suspension up to 1 μm.

2.3. Electrochemical measurements

Electrochemical tests were performed at least by triplicate in a flat-cell using a three-electrodes cell configuration at 49ºC. This value was chosen to mimic the typically used temperature (the most aggressive ones) under CASS tests [13].

A sample area of 1 cm^2 as the working electrode was exposed to 250 mL of quiescent electrolyte. The cell was completed with a saturated

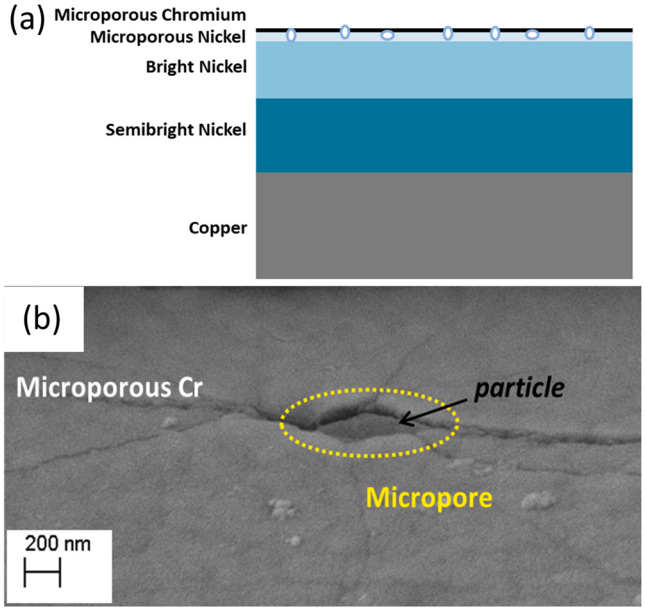

Fig. 1. Microporous nickel-chromium multilayer coating (a) cross section scheme, and (b) Detailed top view of the surface obtained by FE-SEM, where a single micropore (created by the presence of Al_2O_3 particle in the microporous nickel layer) and surrounded by microcracks is observed on the top chromium layer.

calomel electrode (SCE, saturated KCl) and a platinum mesh as the reference and the counter electrodes, respectively. Two types of measurements were carried out using the same VSP-300 Biologic potentiostat: i) single open circuit potential (OCP) measurements with time in naturally aerated electrolytes, and ii) potentiodynamic tests using both naturally aerated (O_2) and deaerated (N_2 atmosphere) electrolytes. The electrochemical test consists of three steps: (1) 1.5 h at OCP measurement, (2) a linear polarisation resistance (LPR) measurement in the potential range ± 10 mV (vs E_{OCP}) at 0.167mVs^{-1} scan rate, and (3) potentiodynamic polarisation scans (also 0.167mVs^{-1} scan rate). The cathodic and anodic branches of the curves were obtained separately: starting from OCP to − 300 mV in the cathodic direction and to 300 mV in the anodic one. The pH, conductivity and O_2 content was measured by a Meter from VWR pHenomenal®.

Corrosion current density (j_{corr}) values were calculated using the Stern-Geary relation [25], given in the following equation:

$$j_{corr} = \frac{\beta_a \beta_c}{2.3 R_p (\beta_c - \beta_a)}$$

where β_a and β_c are the anodic and cathodic Tafel slopes and R_p is the polarisation resistance obtained from the LPR measurement.

2.4. Scanning electrochemical microscope (SECM) experiments

An M470 electrochemical workstation (Bio-Logic) was used to perform the SECM measurements using as a probe a 15 μm diameter platinum microelectrode with RG-value (glass to electrode diameter ratio) of approximately 14.5. The electrochemical cell was completed with a platinum foil and a SCE were employed as counter and reference electrodes, respectively.

Microporous nickel-chromium samples were exposed to the different electrolytes. An area of 0.2 cm^2 was delimited by an insulator (adhesive tape) to perform the SECM experiments. SECM was operated in the competition mode for the detection of dissolved O_2 and H^+ ions, by the oxygen reduction reaction (ORR) and the hydrogen reduction reaction (HRR) at the ultra-microelectrode (UME), respectively. The potential to polarise the UME for each reaction are identified elsewhere ([11,26]), having the following values: (i) ORR: − 0.600 V in the Cl^-_N electrolyte and − 0.250 mV in the Cl^-_H electrolyte, and (ii) HRR: − 0.700 V ([27, 28]).

2.4.1. Approach curves

The approach curves were performed in two different locations: over the adhesive tape (insulating) and over the coatings (active). The curves were obtained after 1 h of immersion to the electrolyte. The SECM probe was placed at a distance close to 200 μm above the surface using a camera. The probe was moved towards the surface by 5 μm steps at a rate of 10 μm/s. The measurements were run at room temperature and repeated at least three times for reproducibility.

The approach curves were carried out using the dissolved O_2 and dissolved H^+ as the redox mediators, applying the potential values mentioned before. The approach curves were normalised by dividing the tip current by the limiting current ($i_{norm} = i/i_{lim}$), and the position dividing the distance by the radius of the UME ($L_{norm}=d/a$).

2.4.2. Area scans

Surface area scans of 500 μm x 500 μm dimension were carried out with the sample under OCP conditions, using a scan rate of 10 μm/s with a probe step distance of 25 μm. The tip-sample distance was fixed at 30 μm to monitor both reactions (O_2 and H^+ reduction) which minimizes the impact of the pH at local scale (i.e., in the corrosion process under study) when ORR is monitored in the UME [29]. The scans were carried at room temperature and repeated at least three times for reproducibility.

3. Results and discussion

3.1. Potentiodynamic polarisation experiments

Potentiodynamic polarisation curves (Fig. 2) were obtained for microporous nickel-chromium coatings exposed to both electrolytes in naturally aerated and deaerated conditions, respectively. The different electrochemical parameters are listed in Table 1. Fig. 2(a) shows the

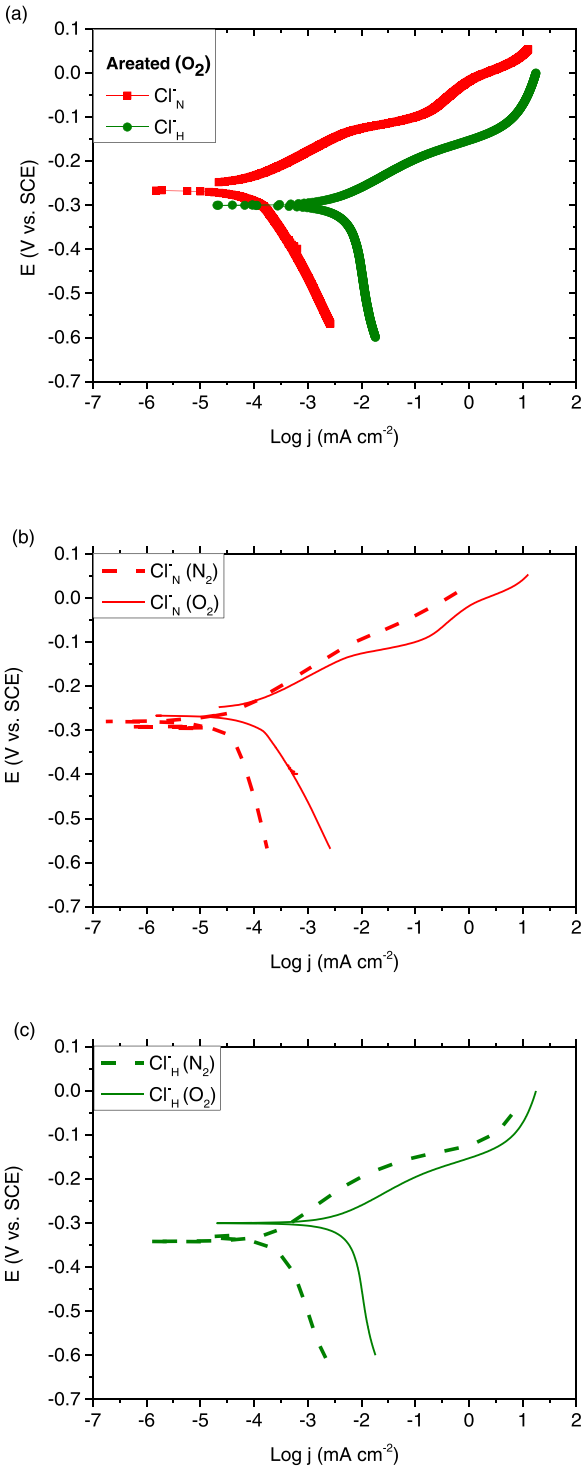

Fig. 2. Potentiodynamic polarisation curve under (a) naturally aerated conditions for Cl^-_N and Cl^-_H electrolytes, and comparison of aerated and unaerated conditions for (b) Cl^-_N electrolyte, and (c) Cl^-_H electrolyte.

Table 1
Electrochemical parameters obtained for microporous nickel-chromium coatings in Cl^-_N and Cl^-_H electrolytes. Data are expressed as mean with standard deviation.

Electrolyte	E_{corr} (mV $_{vs\ SCE}$)	R_p (kohm·cm^2)	β_a (mV·dec^{-1})	$-\beta_c$ (mV·dec^{-1})	j_{corr} (μA·cm^{-2})
$Cl^-_{N\ (O2)}$	-245 ± 17	215.5 ± 62.7	58 ± 6	192 ± 8	0.09 ± 0.04
$Cl^-_{N\ (N2)}$	-270 ± 26	560.0 ± 110.8	81 ± 10	386 ± 3	0.05 ± 0.01
$Cl^-_{H\ (O2)}$	-300 ± 15	6.3 ± 2.9	74 ± 12	536 ± 77	4.51 ± 0.70
$Cl^-_{H\ (N2)}$	-315 ± 15	102.2 ± 12.5	80 ± 4	346 ± 25	0.28 ± 0.01

polarisation curves under aerated conditions for both electrolytes. An active region with a monotonic increase of current during approximately the first 100 mV of anodic overpotential can be observed for the two anodic branches. Considering that the topmost chromium layer always acts as a cathode during exposure to NaCl solutions (having a similar multilayer configuration) [15,30], this behaviour suggests uniform corrosion related to nickel oxidation which is characterised by an anodic slope (β_a) of ≈ 58–81 mVdec^{-1}. At potentials above 100 mV of anodic overpotential, the current increased with a higher rate (smooth change in the slope of the curve) which may be due to the activation of more active corrosion sites favouring the dissolution of the B Ni layer. The main difference between non-acidified (Cl^-_N) and acidified electrolytes is the shift to higher current values of the latter (Table 1). Regarding the cathodic branches of the curves, different trends can be observed under aerated conditions. Although a single slope can be observed for both electrolytes, the sample exposed to the Cl^-_H one shows higher cathodic current values (j_{corr} 4.51 μA·cm^{-2} instead 0.09 μA·cm^{-2}), and higher value of the cathodic slope (536 mV dec^{-1}, Table 1). Finally, the E_{corr} values show a shift to more negative values from − 245 ± 17 mV (Cl^-_N) to − 300 ± 15 mV (Cl^-_H) that might indicate a larger aggressiveness of the electrolyte due to the lower pH value (3.1). These differences observed in the polarisation curves (Fig. 2) confirm that the ORR is influenced by the type of the electrolyte.

On the other hand, the polarisation curves were also measured under deaerated conditions to understand the solely impact of the pH (Fig. 2(b) and (c)). In general, the curves show a shift to more negative E_{corr} potentials (around 15–25 mV). The main differences observed from the curves are regarding the j_{corr} values. The curve obtained (Fig. 2(b)) in the Cl^-_N (N_2) electrolyte showed smooth variations: a decrease of the current density (from 0.09 to 0.05 μA·cm^{-2}) and a more negative E_{corr} (from −245 ± 17 to −270 ± 26 mV) compared to the aerated one. Independently of the presence of oxygen, this electrolyte is showing the lowest j_{corr} values (i.e., lowest aggressiveness). However, if the polarisation curve is obtained in an acidified electrolyte at pH = 3.1 (Cl^-_H) under deaerated conditions (N_2), the impact of O_2 on the corrosion rate seems to be more evident (Fig. 2(c)). In fact, j_{corr} decreases one order of magnitude (from 4.51 to 0.28 μA·cm^{-2}) under N_2.

Results clearly reveal the impact of the pH in the corrosion performance of these coatings.

3.2. Monitoring the reduction reactions by SECM

The early-stage and evolution of the corrosion process were monitored by SECM experiments under OCP conditions for both electrolytes, Cl^-_N and Cl^-_H. The SECM experiments aimed to monitor different reduction reactions that might take place (e.g., ORR and HRR) as a function of the electrolyte with time. In that sense, the SECM was operated in competition mode, and the microelectrode is polarised at the corresponding potential of the reduction of O_2 and H^+. The currents measured at the UME are associated with the concentration of the species available in the sample/electrolyte interface. Corrosion processes (cathodic reactions) occurring on the surface will locally decrease the availability of these species to be reduced by the UME.

3.2.1. SECM approach curves

Normalised approach curves were obtained for each electrolyte over (i) the microporous nickel-chromium surface, and (ii) over the insulator tape delimiting the sample (as inactive substrate). Fig. 3 shows the

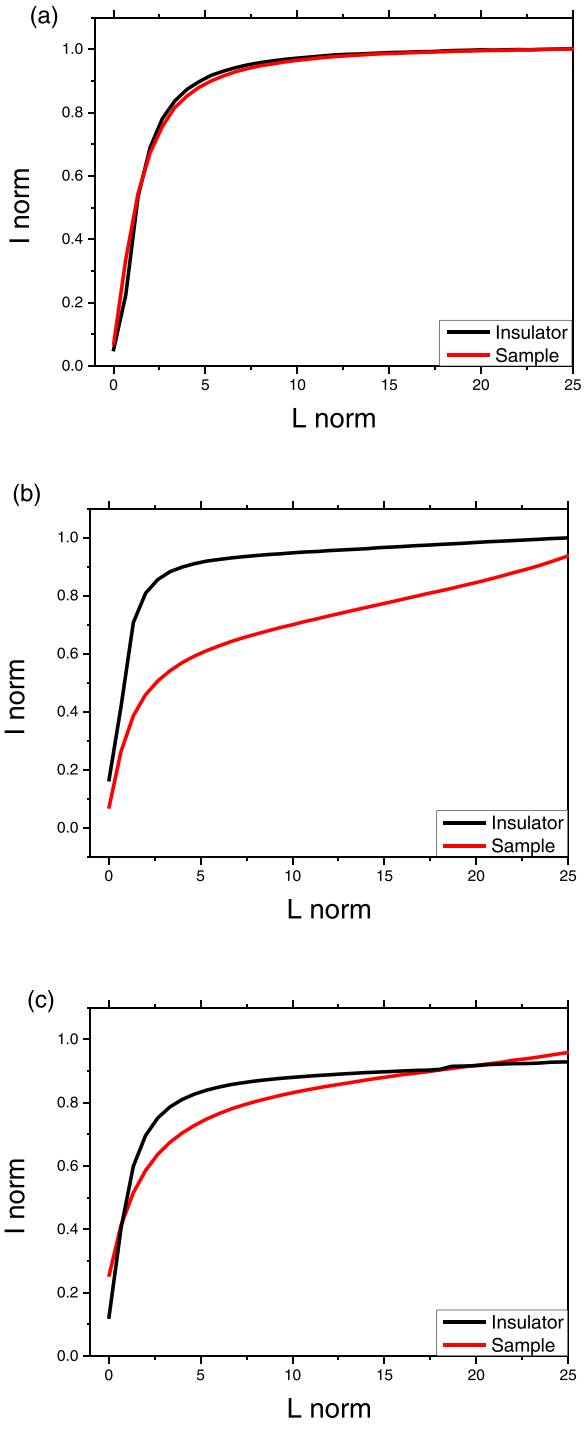

Fig. 3. Approach curves were measured on the insulating substrate (black line) and microporous nickel-chromium sample (red line) immersed in (a) Cl^-_N electrolyte, (b) and (c) in Cl^-_H electrolyte. The UME was polarised using: (i) O_2 as redox mediator at (a) − 0.600 V and (b) − 0.250 V, (ii) H^+ as redox mediator at (c) - 0.700 V.

approach curves of the microelectrode polarised to monitor the different redox species O_2 in Cl^-_N and Cl^-_H electrolytes, and H^+ in Cl^-_H. The approach curves obtained on the insulator (tape) showed negative feedback response for all electrolytes, with a clear transition between the limiting current (plateau at $L_{norm} > 5$) and the sharp decrease. This is the typical response of an inactive surface. In this case, the current is only influenced by the geometrical blockage of the substrate limiting the access of the redox species to the probe [29]. The approach curves measured on the microporous nickel-chromium surface showed different behaviour depending of the solution and the redox species reduced at the probe. In the case of the Cl^-_N electrolyte (Fig. 3(a)) for O_2 reduction, the curve showed exactly the same behaviour as on the insulator substrate. The sample seems not active, and the probe current only decays at the very proximity of the substrate ($L_{norm} < 5$) as a result of the limited diffusion of oxygen. In this case, the dissolved oxygen is purely acting as a redox mediator. The normalised currents close to 1 correspond to the limiting current value, which is related to the concentration of redox species (oxygen) in the bulk.

The response of the probe changed when the approach curve was carried on the sample immersed in the acidified Cl^-_H electrolyte (Fig. 3 (b)). Although there is still an abrupt decay of the current ($L_{norm} < 5$), a constant limiting current is not attained ($L_{norm} > 5$). It indicates that there is less dissolved oxygen available in the solution to undergo the reduction at the probe (already at positions far from the substrate) and therefore, the consumption of oxygen (due to corrosion) from the sample has already started. Then, if the electrolyte is acidified (pH 3.1), the aggressiveness is increased which is in agreement with its largest j_{corr} previously obtained (Table 1).

A similar response occurs in the acidified electrolyte (Cl^-_H) when HRR is the reaction selected at the probe. The approach curve over the sample (Fig. 3(c)) shows a decay of the current already at locations far from the substrate ($L_{norm} > 5$). This confirms that there is consumption of H^+ ions by the substrate as a result of a cathodic reaction due to corrosion.

In summary, the approach curves results demonstrate that the acidification of the chloride-based electrolyte increases the aggressiveness, where early onset of corrosion occurs compared to the neutral electrolyte. For the same immersion time (approx. 1 h), a consumption of the redox species was detected only in the case of Cl^-_H electrolyte. Furthermore, it is possible to confirm that both, O_2 molecules and H^+ ions are involved in the cathodic processes taking place during corrosion.

3.2.2. SECM area scans

SECM area scans were performed to monitor the cathodic process under both electrolytes, Cl^-_N and Cl^-_H Fig. 4 shows the SECM maps by operating in competition mode to monitor with time the oxygen depletion due to the cathodic reaction in the neutral Cl^-_N electrolyte. There is no sign of oxygen consumption in early times of exposure (1 h, Fig. 4(a)) as well as after 5 days (Fig. 4(b)). Currents values are in the magnitude range expected for the tip-sample distance used in the experiments (30 μm). The small variation may be associated with the tilt of the sample. After 8 days of exposure, there is a considerable change in the magnitude of the current to lower values ($< 10^{-9}$ A, Fig. 4(c)). This is related to less dissolved oxygen available for the reaction at the microelectrode, indicating that corrosion processes are taking place. Furthermore, the map showed zones (upper part and bottom-left part) with more pronounced depletion of oxygen (current scale into the range of 8.4 – 9.9 10^{-10} A) which can be first evidences of localised cathodic areas. The presence of these localised cathodes became more evident after 12 days of exposure (see circles in Fig. 4(d)). Well-defined cathodic sites are detected at two different spots (1) X = 400 μm, Y = 200 μm; and (2) X = 250 μm, and Y = −150 μm, respectively.

In overall, under Cl^-_N electrolyte there is no evidence of corrosion process on the microporous nickel-chromium coatings during the first days after immersion. It is only after between 8 and 12 days that significant depletion of oxygen related to the cathodic process is detected. The activity showed a localised behaviour. The slow corrosion kinetic is associated to the low aggressiveness of the solution, especially at room

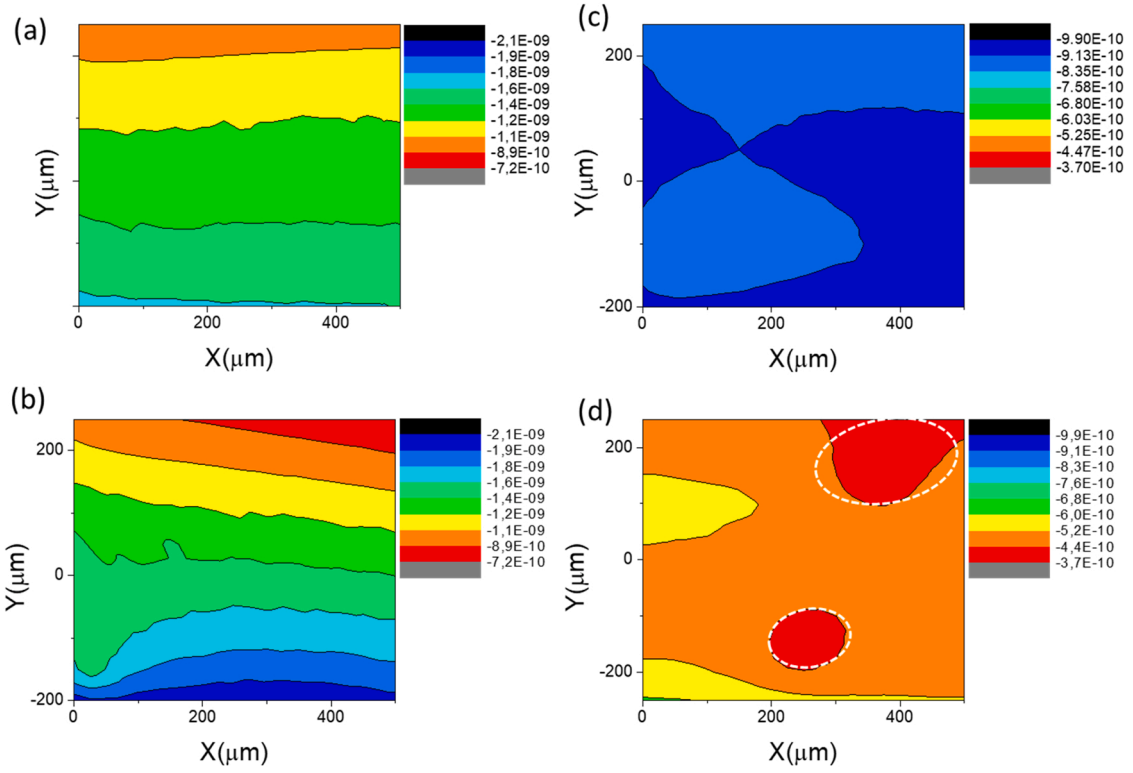

Fig. 4. SECM maps monitoring oxygen in competition mode during exposure to Cl^-_N electrolyte: (a) 1 h, (b) 5 days, (c) 8 days, and (d) 12 days. The UME was polarised at − 0.600 V. Current scale: Amperes (A).

temperature, as was also observed from the potentiodynamic polarisation results (Fig. 2, Table 1). The observation that no activity is detected on the first day of immersion explains that there are no differences between the approach curves measured on the sample and the insulating tape (Fig. 3).

Similar SECM scan measurements monitoring oxygen depletion were carried out in the Cl^-_H electrolyte. SECM maps obtained after 1 h and 24 h of exposure (Fig. 5(a) & (b)) did not show localised activity but the current values seem to decrease more rapidly between those instants. This indicates that there is a decay of dissolved oxygen in the solution and also corroborate the results from the approach curves in Fig. 3(b). Localised cathodic activity is detected after 48 h of exposure in an acidified environment (the upper-left part of the SECM map in Fig. 5(c)) and remained after 72 h of immersion (Fig. 5(d)). As expected, the corrosion propagation in the acidified electrolyte (Cl^-_H one) was much faster according to the higher current density values obtained from the potentiodynamic polarisation experiments (Table 1).

In order to confirm H^+ reduction (acidified medium) is also contributing to the corrosion process (Fig. 2, Fig. 3), SECM maps (Fig. 6) were obtained by competition mode monitoring the HRR at the probe. Fig. 6(a) was recorded immediately after obtaining Fig. 5(c). It shows strong and localised depletion of H^+ ions in the same location the oxygen depletion was detected (Fig. 5(c)). With longer immersion time (72 h) the site showed still activity (Fig. 6(b)). These results confirm the presence of well-defined and localised cathodic sites after approximately 48 h of exposure and that O_2 and H^+ species are involved in the cathodic reduction reactions during corrosion.

In summary, SECM area scan experiments allowed monitoring the corrosion processes at localised scale once it has started. In agreement with the potentiodynamic tests (Fig. 2), a much shorter time was required to detect early-stage corrosion for the electrolytes with higher aggressiveness (Table 1) obtaining the same classification in terms of aggressiveness: $Cl^-_N << Cl^-_H$.

3.3. Cross-section characterisation

3.3.1. Non-acidified electrolyte (Cl^-_N)

According to the different aggressiveness of the electrolytes, samples were exposed for a period of 22 h to the Cl^-_H electrolyte and 92 h to the Cl^-_N electrolyte, both at 49ºC. The corrosion damages underneath the chromium layer have been studied (cross-section micrographs) by FE-SEM. In our previous work [10], only the average height and width of the active sites detected at that particular time (i.e., 22 h) was quantified. In this current research, a more detailed analysis has been carried out by selecting different exposure times for each electrolyte (Fig. 7 and Fig. 8). It is important to notice that the terminology "active sites" has been used rather than the term pits (already used for similar decorative nickel-chromium systems) [31,32] to avoid misunderstanding with the "pitting" phenomena studied in passive metals and their alloys [33].

Fig. 7 shows micrographs at 22, 36 and 92 h of exposure to the Cl^-_N electrolyte. In addition, Table 2 lists the values of parameters such as width, height their ratio (width/height) for all electrolytes. Fig. 7(a) shows an active site with a hemispherical shape (around 4.0 μm width and 3.2 μm height, Table 2), indicating an isotropic growth after 22 h of exposure. As expected, it seems that the corrosion front went throughout the MPS Ni layer before reaching the B Ni layer. Apparently, only a few sites were developed (hemispherical shape) due to corrosion. They seem to be located in the B Ni layer preserving the integrity of the MPS Ni layer. If the exposure time increases up to 36 h, the corrosion front has dissolved the B Ni layer, reaching the SB Ni one (Fig. 7(b)). At this stage, the isotropic growth is getting lost (width:height = 1.77 at 36 h instead of 1.25 at 22 h, Table 2) and the corrosion progresses laterally throughout the B Ni layer (elliptical shape). Moreover, the MPS Ni layer seems to be partially corroded in the central part of the active site. Considering a thickness value of B Ni layer is around 10.7 ± 1.4 μm, the height (11.7 μm, Table 2) of this active site may indicate that certain corrosion has also occurred in MPS Ni layer. However, this active site is still considered as "closed one" (terminology previously used [10]) because it is maintaining the integrity of the thin chromium layer.

In order to promote larger damages under this Cl^-_N electrolyte, the

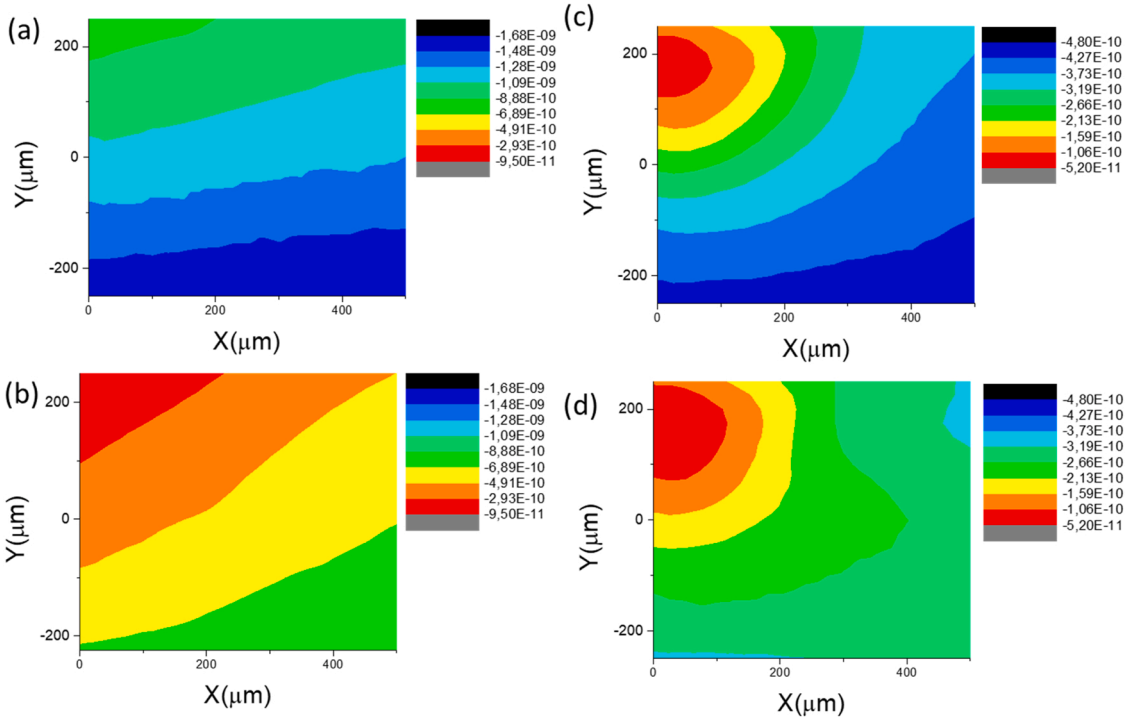

Fig. 5. SECM maps monitoring oxygen in competition mode during exposure to Cl^-_H electrolyte during: (a) 1 h, (b) 24 h, (c) 48 h, and (d) 72 h. The UME was polarised at − 0.250 V. Current scale: Amperes (A).

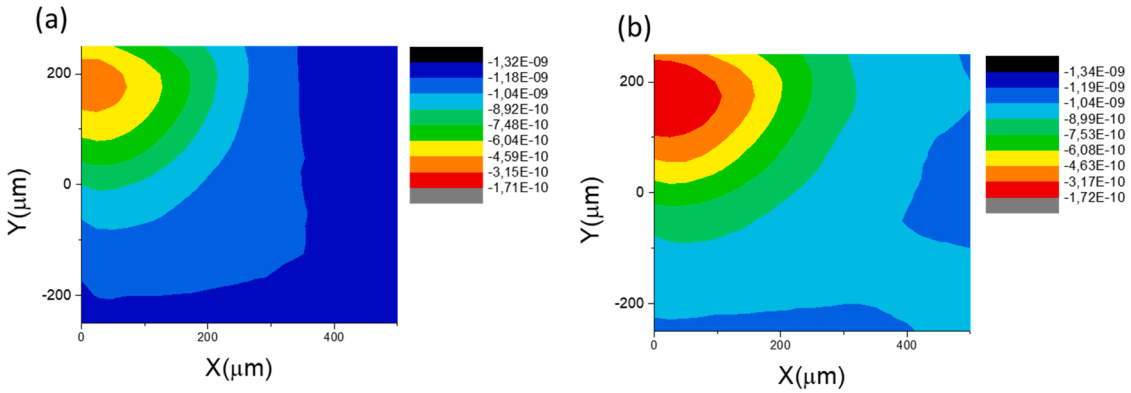

Fig. 6. SECM maps monitoring H^+ in competition mode during exposure to Cl^-_H electrolyte during: (a) 48 h, and (b) 72 h. The UME was polarised at − 0.700 V. Current scale: Amperes (A).

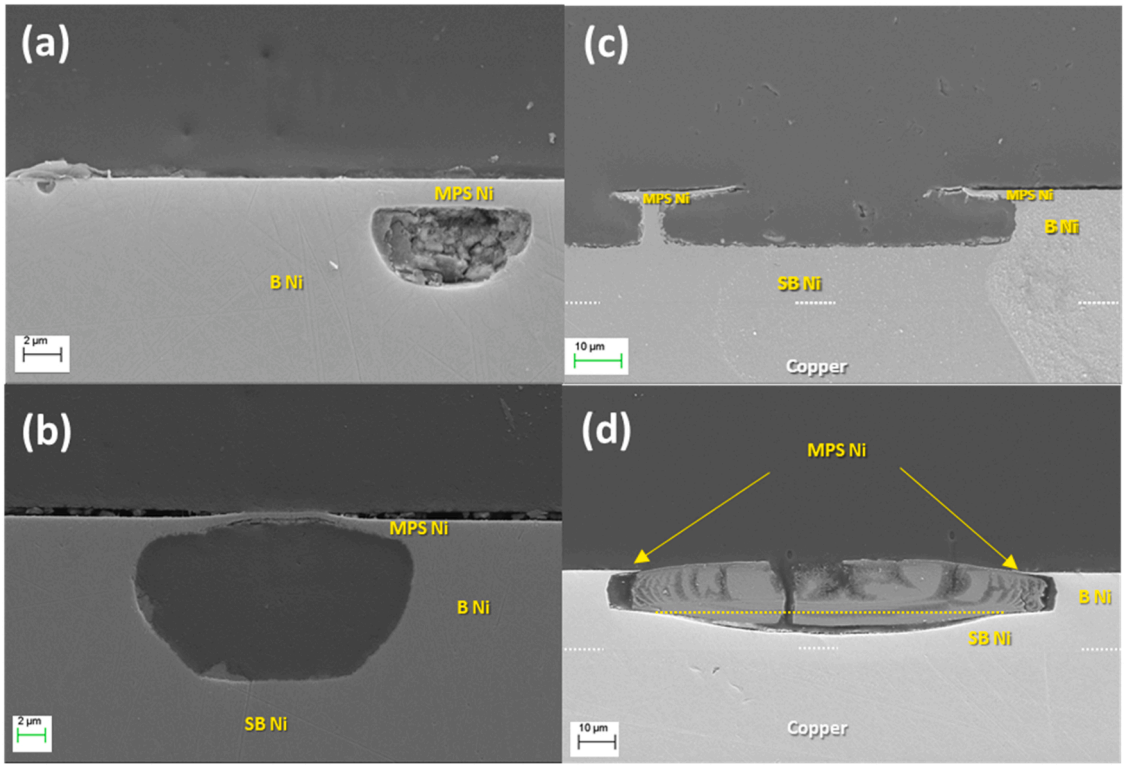

Fig. 7. FE-SEM micrographs showing the evolution with time of active sites after exposure to aerated Cl^-_N electrolyte: (a) 22 h, (b) 36 h, (c) & (d) 92 h (≈ 4 days).

exposure time was increased up to 92 h (≈4 days), where two types of active sites were observed. Fig. 7(c) indicates a clear transition from an elliptical shape (Fig. 7(b)) to a rectangular one, where not only the active site shape has changed, but also the MPS Ni layer is completely attacked. Here, the active site can be classified as "open" (76.7 μm width and 14.0 μm height), where the chromium layer has also disappeared due to the corrosion of the MPS Ni layer. On the other hand, Fig. 7(d) also shows other typical active sites after 92 h of exposure. In this case, an elliptical shape merged with rectangular can be observed, having width values of 121.7 μm and height of 17.5 μm. This latter large value in depth indicates that the corrosion of the SB Ni layer has occurred which is confirmed visually due to the elliptical shape of the cross-section (see dot line). It seems that the SB Ni layer is prone to be corroded if the width of the active site is above a certain threshold (at least beyond 76.7 μm, Fig. 7(c)), whilst independently of the width, the MPS Ni layer is always corroded (Fig. 7(c) & (d)).

3.3.2. *Acidified electrolyte (Cl^-_H)*

Fig. 8(a) shows an active site with a hemispherical shape after 3.5 h of exposure to Cl^-_H electrolyte. Although it is larger (around 9.6 μm width and 6.9 μm height, Table 2) than the one created after 22 h of exposure to Cl^-_N electrolyte (4.0 μm width and 3.2 μm height, Fig. 7(a)), both have a similar shape. Then, it can be assumed that both active sites underwent an isotropic growth (width:height ratio between 1.25 and 1.39) but at different corrosion rates. If the time of exposure is increased up to 8 h (Fig. 8(b)), not only the shape but also the width/height ratio are maintained (1.52, Table 2), indicating homogeneous progress of the corrosion front. Finally, there is an abrupt change in the shape that goes from hemispherical to elliptical after 22 h of exposure (Fig. 8(c)). Once the penetration depth reaches the SB Ni layer, the corrosion of the MPS Ni layer occurs together with the lateral corrosion of the B Ni layer and certain (as well as certain corrosion of the SB Ni layer). At this time, the width/height ratio is still maintained (1.80) which is typical of isotropic growth. Therefore, despite having higher corrosion rate at pH = 3.1 (Cl^-_H

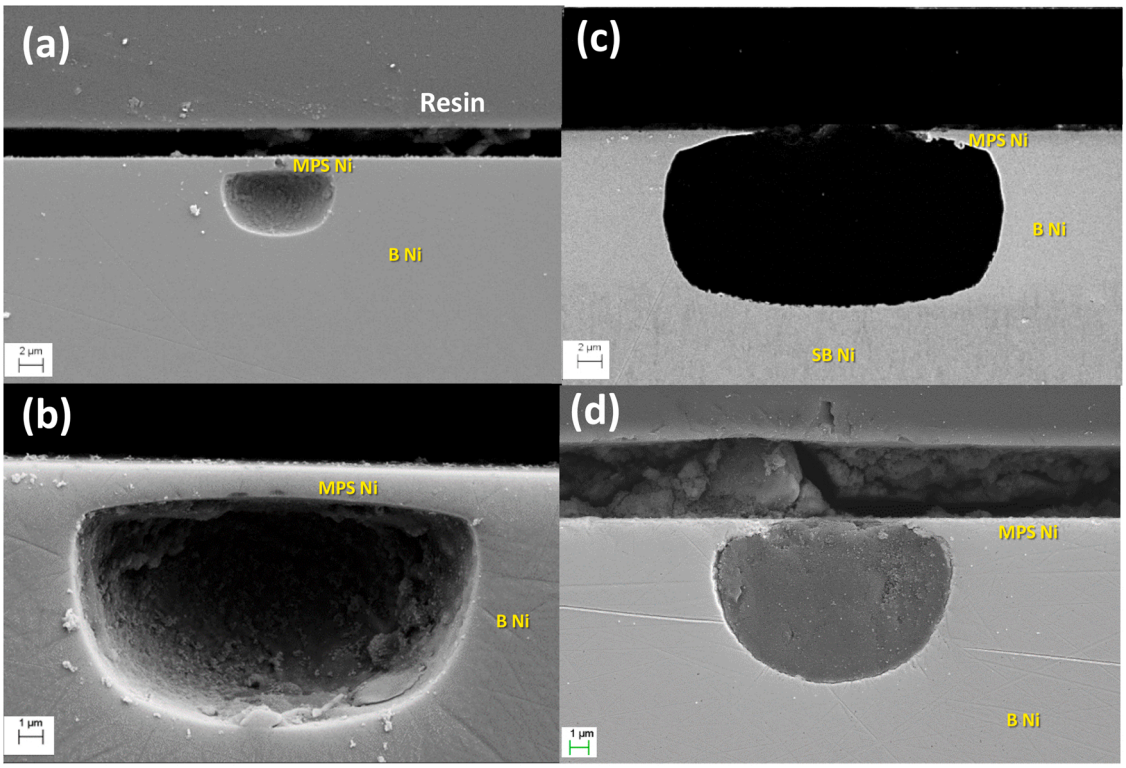

Fig. 8. FE-SEM micrographs showing the evolution with time of active sites after exposure to Cl^-_H electrolyte in aerated conditions (a) 3.5 h, (b) 8 h, and (c) 22 h, and (d) deaerated one after 22 h.

Table 2
Features of the active sites created in microporous nickel-chromium coatings after different times of exposure in both electrolytes, including deaerated conditions for Cl^-_H electrolyte.

Electrolyte	Time (h)	Width (µm)	Height (µm)	Ratio Width: Height
$Cl^-_{N\ (O2)}$ (Fig. 7)	22	4.0	3.2	1.25
	36	20.7	11.7	1.77
	92	76.7	14.0	5.47
	92	121.7	17.5	6.95
$Cl^-_{H\ (O2)}$ (Fig. 8(a), (b) & (c))	3.5	9.6	6.9	1.39
	8.0	16.6	10.9	1.52
	22	28.5	15.8	1.80
$Cl^-_{H\ (N2)}$ (Fig. 8(d))	22	12.6	8.9	1.41

electrolyte), a similar corrosion mechanism is observed in both electrolytes, where the three nickel layers were attacked. Theoretically, the MPS Ni layer was supposed behave as cathode versus B Ni one [34] but independently of the electrolyte (Cl^-_N or Cl^-_H), it has been extensively corroded. In order to explain it, samples were exposed during 22 h under deaerated conditions in the Cl^-_H electrolyte (Fig. 8(d)). The cross-section images reveal much lower damage under N_2 than under O_2 (Fig. 8(c)) which is in agreement with j_{corr} values (0.28 µA·cm^{-2} instead 4.51 µA·cm^{-2}, Table 1). A typical hemispherical shape can be observed (12.6 µm width and 8.9 µm height, Fig. 8(d)) due to an isotropic growth (1.41 ratio width:height, Table 2). Interestingly, the MPS Ni layer has already been corroded here, in contrast to active sites of similar dimensions (16.6 µm width and 10.9 µm height) but obtained under aerated conditions after 8 h of exposure in the same electrolyte (Fig. 8 (b)). This finding is in agreement with the hypothesis that considers oxygen depletion (e.g. deaerated scenario) inside of the active site [5, 33] as one of the main reason to trigger the polarity reversal between Ni B and MPS Ni layers, favouring the corrosion of the latter under this scenario.

In summary, different aggressiveness it has been observed as a function of the electrolyte (Cl^-_N << Cl^-_H), where opened ones (without top chromium layer) are usually developed with the time of exposure. An isotropic growth (hemispherical shape) occurs at the beginning of the corrosion process and later on, the active site evolves to an elliptical shape due to: (i) the widening of the active site by the lateral dissolution of B Ni layer, (ii) the corrosion of the MPS Ni layer, and (iii) the partial attack of the SB Ni layers. Indeed, larger exposure time (e.g., 92 h in Cl^-_N electrolyte) facilitates the formation of rectangular active sites (or elliptical merged with rectangular).

3.4. Corrosion in Cl^-_H electrolyte: impact of the pH

It has been observed that O_2 and H^+ are involved in the corrosion process of microporous nickel-chromium coatings under an acidified electrolyte (Cl^-_H, Fig. 2(c)). The O_2 reduction in a neutral electrolyte (Cl^-_N) usually proceeds along with one, or both, of the following two pathways [35,36]:

(i) two consecutive two-electron steps to hydrogen peroxide species:

$$O_2 + H_2O + 2e^- \rightarrow HO_2^- + OH^- \quad E_{SHE} = -0{\cdot}065\ V \tag{1}$$

$$HO_2^- + H_2O + 2e^- \rightarrow 3OH^- \quad E_{SHE} = 0.867\ V \tag{2}$$

or (ii) with a direct four-electron step:

$$O_2 + 2\,H_2O + 4e^- \rightarrow 4OH^- \quad E_{SHE} = 0.401\ V \tag{3}$$

In contrast, the following pathways can occur under an acidic medium such Cl^-_H electrolyte [37]:

$$O_2 + 4\,H^+ + 4e^- \rightarrow 2\,H_2O \quad E_{SHE} = 1{\cdot}229\ V \tag{4}$$

$$O_2 + 2\,H^+ + 2e^- \rightarrow H_2O_2 \quad E_{SHE} = 0.695\ V \tag{5}$$

where the two-electron pathways generate unstable peroxides as products. These species can further be reduced to water in the acidic medium:

$$H_2O_2 + 2\,H^+ + 2e^- \rightarrow 2\,H_2O\ E_{SHE} = 1{\cdot}776\ V \quad (6)$$

or it decomposes by a disproportionation:

$$2\,H_2O_2 \rightarrow 2\,H_2O + O_2 \quad (7)$$

Considering that an acidic pH is used, the following reduction reaction can also occur (HRR, Eq. 8):

$$2\,H^+ + 2e^- \rightarrow H_2\ E_{SHE} = 0.0\ V \quad (8)$$

Although it seems that the ORR (following Eqs. (4), (5)) may be controlling the corrosion rate according to the standard electrode potential values, there are certain contribution of the pH to the overall corrosion phenomena. In order to estimate it, semi-quantitative analysis was made from the polarisation curves comparing the j_{corr} values (Fig. 2 (c), Table 1). The synergy between H^+ and O_2 provides large j_{corr} values (4.51 $\mu A{\cdot}cm^{-2}$). The impact of oxygen can be estimated from the curve under deaerated conditions (j_{corr} = 0.28 $\mu A{\cdot}cm^{-2}$), indicating a difference above one order of magnitude. On the other hand, in order to isolate the hypothetical contribution of the pH without the effect of O_2 (to avoid the reactions from Eq. (4) & (5)), the j_{corr} under deaerated conditions for both electrolytes (Cl^-_N and Cl^-_H,) can be compared (0.05 $\mu A{\cdot}cm^{-2}$ vs. 0.28 $\mu A{\cdot}cm^{-2}$). Once again, the current density values

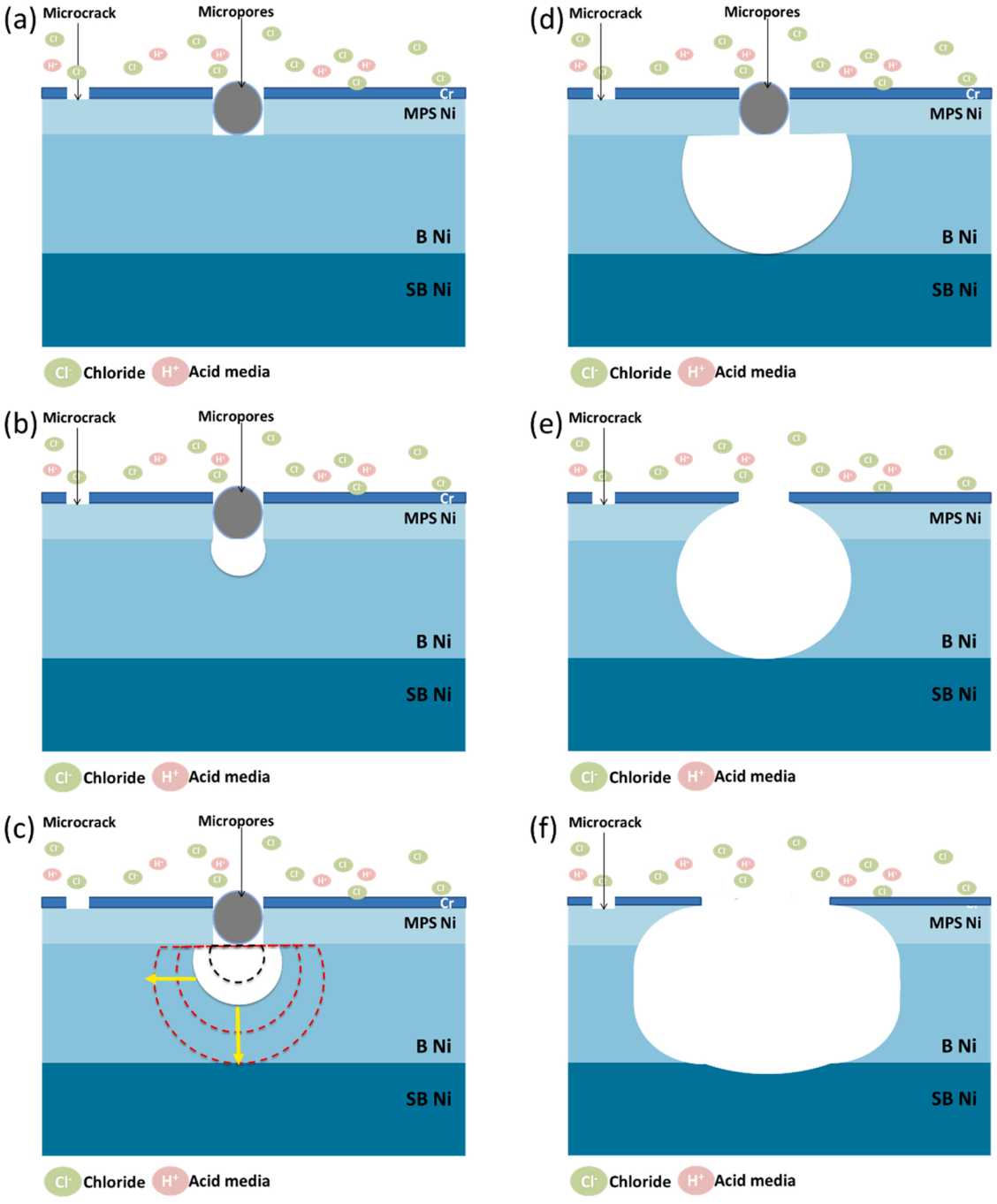

Fig. 9. Schematic representation of the corrosion mechanism of microporous nickel-chromium coatings exposed to chloride-based electrolytes (independently of the acidified pH): (a) intact multilayer system, (b) corrosion goes throughout the B Ni layer, (c) an isotropic growth occurs once the active site is located in the B Ni layer, (d) the active site reaches the SB Ni layer (e) the corrosion mechanism is modified and the MPS Ni layer is being attacked, and (f) widening of the corrosion site, triggering also the corrosion attack of the SB Ni layer.

differ five times which confirms the impact of the pH in terms of corrosion rate for these decorative coatings. Then, this finding can justify the large attack obtained under deaerated conditions (no influence of O_2) in the Cl^-_H electrolyte after 22 h of exposure (j_{corr} = 0.28 μA·cm^{-2}, 12.6 μm width, and 8.9 μm height, Fig. 8(d)) compared to the one obtained in the Cl^-_N electrolyte under aerated ones (j_{corr} = 0.09 μA·cm^{-2}, 4.0 μm width, and 3.2 μm height, Fig. 7(a)) at the same time of exposure (22 h).

On the other hand, the SECM maps have shown the consumption of different redox species (i.e., H^+ and O_2) by the sample in the Cl^-_H electrolyte. The impact of the pH was also proven by SECM approach curves, where lower current values than expected (compared to Fig. 3(a) in Cl^-_N electrolyte) were measured in the UME: larger consumption of O_2 occurred at $L_{norm} = 4$ ($I_{norm} = 0.57$, Fig. 3(b)) by the sample for ORR and larger consumption of H^+ at same distance ($L_{norm} = 4$, $I_{norm} = 0.70$, Fig. 3(c)) for HRR.

As a summary, H^+ can be consumed in several reactions (Eqs. 4, 5, 6 and 8) and the impact of the pH in the corrosion rate has been confirmed either by SECM (maps and approach curves) or potentiodynamic polarisation measurements. However, it seems that such an impact does not affect the corrosion mechanism of microporous nickel-chromium coatings as has been described below.

3.5. Corrosion mechanism of microporous nickel-chromium coatings

In general, microporous nickel-chromium systems (also having microcracks) are designed to guide and maintain the hidden corrosion front, minimising the visual impact on the surface. Theoretically, those three nickel layers were chosen for having different electrochemical potentials and once the galvanic coupling occurs, the less noble layer (i.e., B Ni) is anodically polarised if a chloride-based electrolyte using cupric ions is used [38]. However, this theoretical scenario is not maintained for Cl^-_N and Cl^-_H electrolytes, where the corrosion not only occurs in the B Ni layer but also in the other two: it was mainly affecting the MPS Ni layer but not exclusively because SB Ni layer was also attacked in a lower extent. Therefore, according to the findings of this paper and independently of the pH, the following corrosion mechanism can be established for both electrolytes despite having different corrosion rates (Fig. 9):

(i) The initiation of the corrosion occurs throughout micro-discontinuities such as micropores but not exclusively (e.g., the microcracks are also the preferential pathway to the access of the electrolyte, Fig. 9(a)).
(ii) Once the B Ni layer has been reached by the corrosion front, the progress of corrosion remains located in this single layer (Fig. 9 (b)), maintaining almost an isotropic growth (width/height ratio < 2) along with this layer Fig. 9(c).
(iii) The isotropic growth is maintained until the corrosion front reaches the surface of the SB Ni layer (Fig. 9(d)). At this moment, independently of the aggressiveness of the electrolyte, there is a change in the corrosion mechanism and the active site is forced to grow in a different direction. It is due to the isotropic growth being hindered in depth by the presence of the SB Ni layer (not corroded yet).
(iv) From now on, the corrosion starts to occur in the opposite direction, i.e., the MPS Ni layer is attacked (Fig. 9(e) and becomes to behave as the anode for both, Cl^-_N and Cl^-_H electrolytes. Therefore, to temporarily maintain the isotropic growth, Fig. 9(e) not only shows the attack of the MPS Ni layer but also certain lateral corrosion of the B Ni layer.
(v) At certain point, the SB Ni layer is also corroded but to a much lower extent (Fig. 9(f)). Finally, in addition to the attack of the MPS and SB Ni layers, the lateral corrosion of the B Ni layer promotes the anisotropic growth of the active site.

4. Conclusions

The corrosion of nickel-chromium systems has been explored using conventional and localised electrochemical techniques at different pH. The main findings are the following:

- SECM approach curves and maps were carried out to monitor the species (i.e.,O_2 and H+) involved in the cathodic reactions governing the corrosion process at localised scale. Localised cathodic sites were distinguished after 48 h for Cl^-_H electrolyte and 192 h (≈8 days) for Cl^-_N electrolyte, respectively.
- Potentiodynamic polarisation curves (at 49ºC) were crucial to validate the SECM results at room temperature in terms of aggressiveness, showing that the impact of the pH was solely affecting to the corrosion rate rather than to the corrosion mechanism.
- The corrosion mechanism has been elucidated at early-stage corrosion and during the corrosion propagation. Initially, corrosion solely occurred into the B Ni layer under isotropic growth. Once the active site reached the boundary with the SB Ni layer, the corrosion mechanism was modified and MPS Ni layer was also attacked. The widening of the active site (i.e. lateral corrosion of the B Ni layer) and the attack of the SB Ni layer took place during the propagation of anisotropic active sites.

CRediT authorship contribution statement

Jesús Manuel Vega: Conceptualization, Methodology, Formal analysis, Investigation, Visualization, Supervision, Project administration, Funding acquisition, Data curation, Writing - original draft, Writing - review & editing. **Larraitz Ganborena:** Methodology, Formal analysis, Investigation, Visualization, Data curation, Writing - review & editing. **Yaiza Gonzalez-Garcia:** Formal analysis, Investigation, Supervision, Data curation, Methodology, Writing - original draft, Writing - review & editing. **Berkem Özkaya:** Resources, Writing – review & editing, Supervision. **Hans-Jürgen Grande:** Resources, Writing – review & editing, Funding acquisition. **Eva García-Lecina:** Conceptualization, Writing – review & editing, Supervision, Project administration, Funding acquisition.

Declaration of Competing Interest

The authors declare that they have no known competing financial interests or personal relationships that could have appeared to influence the work reported in this paper.

Data availability

The raw/processed data required to reproduce these findings cannot be shared at this time as the data also forms part of an ongoing study.

Acknowledgements

The authors would like to thank the financial support and samples provided by ATOTECH Deutschland GmbH. This work was partially supported by the Spanish Government (PID2020-116844RB-C22 and CER-20191003). Dr. Yaiza Gonzalez-Garcia acknowledges the funding from COST (European Cooperation in Science and Technology) to carry out an STSM within the framework of the COST action MP 1407.

Data availability

The raw/processed data required to reproduce these findings cannot be shared at this time as the data also forms part of an ongoing study.

References

[1] C. Terrien, Decoration with metallic luster, BUP 105 (2011) 15–51.
[2] D.C. Rich, A review of solid-state lighting and its impact on the marketing and production of decorative coatings, J. Coat. Technol. Res. 13 (2016) 1–9, https://doi.org/10.1007/s11998-015-9704-1.
[3] R. Constantin, P.-A. Steinmann, C. Manasterski, Decorative PVD coatings, in: Nanomater. Surf. Eng., ISTE Ltd., 2010, pp. 109–161.
[4] V. James, P. Leger, Modern formulations for decorative paints and coatings, Surf. Coat. Aust. 49 (2012) 20–24.
[5] L. Pohlmann, G. Bauer, P. Hartmann, P. Wachter, C. Donner, Oscillatory passive active transition during the corrosion in nickel chromium layer systems, J. Solid State Electrochem. 17 (2013) 489–496, https://doi.org/10.1007/s10008-012-1949-3.
[6] B.B. Knapp, Research and decorative coatings, Plat. Surf. 65 (1978) 24–30.
[7] J.K. Dennis, T.E. Such, Nickel and Chromium Plating, Butterworth and Co. Limited, 1993.
[8] J.F. Vogt, R.J. Herbert, U.S. patent, 2,635,075, 1953.
[9] L. Ganborena, J.M. Vega, B. Özkaya, H.J. Grande, E. García-Lecina, An SKP and EIS study of microporous nickel-chromium coatings in copper containing electrolytes, Electrochim. Acta 318 (2019) 683–694, https://doi.org/10.1016/j.electacta.2019.05.108.
[10] L. Ganborena, B. Özkaya, M. García, H.-J. Grande, E. García-Lecina, J.M. Vega, Corrosion mechanism of microporous nickel-chromium coatings: part I. Impact of cupric ions on nickel layers, J. Electrochem. Soc. 169 (2022), 021503, https://doi.org/10.1149/1945-7111/ac4f78.
[11] L. Ganborena, Y. Gonzalez-Garcia, B. Özkaya, M. García, E. García-Lecina, J. M. Vega, Corrosion mechanism of microporous nickel-chromium coatings: part II. SECM study monitoring Cu2+ and oxygen reduction, J. Electrochem. Soc. 169 (2022), 021509, https://doi.org/10.1149/1945-7111/ac554a.
[12] J. León, S. Pletincx, H. Terryn, B. Özkaya, E. García-Lecina, J.M. Vega, Unravelling the Fe effect on the corrosion of chromium coatings: chemical composition and semiconducting properties, J. Electrochem. Soc. 168 (2021), 121501, https://doi.org/10.1149/1945-7111/ac3ac0.
[13] ASTM B 368 – 97, Standard Test Method for Copper-Accelerated Acetic Acid-Salt Spray (Fog) Testing (CASS Test) 1, Annu. B. ASTM Stand. i (2011) 1–5. doi: 10.1520/B0368-09.2.
[14] D.L. Snyder, Decorative chromium plating basics, Met. Finish. 110 (2012) 14–21, https://doi.org/10.1016/S0026-0576(13)70110-7.
[15] R. Tremmel, Methods to Improve the corrosion performance of microporous nickel deposits, Plat. Surf. Finish. (1996) 24–28.
[16] G.A.Di Bari, Electrodeposition of nickel, Mod. Electroplat. Fifth Ed. (2010) 79–114, https://doi.org/10.1002/9780470602638.ch3.
[17] X. Yang, R. Zeng, X. Fu, X. Wang, J. Zhou, L. Yu, Influence of the Cu content on the electrochemical corrosion performances of Ni60 coating, Corros. Sci. 205 (2022), 110408, https://doi.org/10.1016/J.CORSCI.2022.110408.
[18] D. Filotás, B.M. Fernández-Pérez, J. Izquierdo, A. Kiss, L. Nagy, G. Nagy, R. M. Souto, Improved potentiometric SECM imaging of galvanic corrosion reactions, Corros. Sci. 129 (2017) 136–145, https://doi.org/10.1016/J.CORSCI.2017.10.006.
[19] D. Filotás, B.M. Fernández-Pérez, J. Izquierdo, L. Nagy, G. Nagy, R.M. Souto, Novel dual microelectrode probe for the simultaneous visualization of local Zn2+ and pH distributions in galvanic corrosion processes, Corros. Sci. 114 (2017) 37–44, https://doi.org/10.1016/J.CORSCI.2016.10.014.
[20] J.A. Ramírez-Cano, L. Veleva, R.M. Souto, B.M. Fernández-Pérez, SECM study of the pH distribution over Cu samples treated with 2-mercaptobenzothiazole in NaCl solution, Electrochem. Commun. 78 (2017) 60–63, https://doi.org/10.1016/j.elecom.2017.04.005.
[21] C. Blanc, N. Pébère, B. Tribollet, V. Vivier, Galvanic coupling between copper and aluminium in a thin-layer cell, Corros. Sci. 52 (2010) 991–995, https://doi.org/10.1016/J.CORSCI.2009.11.023.
[22] A.M. Simões, D. Battocchi, D.E. Tallman, G.P. Bierwagen, SVET and SECM imaging of cathodic protection of aluminium by a Mg-rich coating, Corros. Sci. 49 (2007) 3838–3849, https://doi.org/10.1016/J.CORSCI.2007.03.045.
[23] A.M. Simões, A.C. Bastos, M.G. Ferreira, Y. González-García, S. González, R. M. Souto, Use of SVET and SECM to study the galvanic corrosion of an iron–zinc cell, Corros. Sci. 49 (2007) 726–739, https://doi.org/10.1016/J.CORSCI.2006.04.021.
[24] J. Kwak, A.J. Bard, Scanning electrochemical microscopy. apparatus and two-dimensional scans of conductive and insulating substrates, Anal. Chem. 61 (1989) 1794–1799, https://doi.org/10.1021/ac00192a003.
[25] M. Stern, A.L. Geary, Electrochemical polarization, J. Electrochem. Soc. 104 (1957) 559, https://doi.org/10.1149/1.2428653.
[26] L. Ganborena, Novel insights into the corrosion mechanism of decorative multilayer nickel-chromium coatings on ABS: towards a correlation between CASS and electrochemical tests, UPV, 2020.
[27] H. Zhao, J. Chang, A. Boika, A.J. Bard, Electrochemistry of high concentration copper chloride complexes, Anal. Chem. 85 (2013) 7696–7703, https://doi.org/10.1021/ac4016769.
[28] C.P. De Leon, F.C. Walsh, Research and development techniques 1: potentiodynamic studies of copper metal deposition, Trans. Inst. Met. Finish. 81 (2003) 95–100, https://doi.org/10.1080/00202967.2003.11871523.
[29] L.C. Abodi, Y. Gonzalez-Garcia, O. Dolgikh, C. Dan, D. Deconinck, J.M.C. Mol, H. Terryn, J. Deconinck, Simulated and measured response of oxygen SECM-measurements in presence of a corrosion process, Electrochim. Acta 146 (2014) 556–563, https://doi.org/10.1016/j.electacta.2014.09.010.
[30] M. Barnstead, J. Schweitzer, W. Schumacher, Investigations into the performance of multi-layer nickel coatings in both CASS and exhaust gas corrosion testing, Plat. Surf. Finish. (2010) 30–36.
[31] S.R. Maloof, The electrochemical behavior of decorative nickel-chromium coatings in 3% NaCl under porentiostaric conditions, J. Electrochem. Soc. 116 (1969) 1293, https://doi.org/10.1149/1.2412304.
[32] G.N. Flint, S.H. Melbourne, The corrosion of decorative nickel + chromium coatings: a metallographic and potential study, Trans. IMF 38 (1961) 35–44, https://doi.org/10.1080/00202967.1961.11869817.
[33] G.S. Frankel, Pitting corrosion of metals, J. Electrochem. Soc. 145 (1998) 2186, https://doi.org/10.1149/1.1838615.
[34] R. Tremmel, Methods to Improve the corrosion performance of microporous nickel deposits, Plat. Surf. Finish. 83 (1996) 24–28.
[35] Z. Pilbáth, L. Sziráki, The electrochemical reduction of oxygen on zinc corrosion films in alkaline solutions, Electrochim. Acta 53 (2008) 3218–3230, https://doi.org/10.1016/j.electacta.2007.11.056.
[36] P. Delahay, A polarographic method for the indirect determination of polarization curves for oxygen reduction on various metals I. Description of the metho-case of platinum, J. Electrochem. Soc. 97 (1950) 198–204.
[37] J. Bard, A.J. Parsons, R. Jordan, Standard Potentials in Aqueous Solutions, New York, 1985.
[38] G.A. Di Bari, Electrodeposition of nickel, in: Mod. Electroplat., fifth ed., 2010, pp. 79–114. doi:10.1002/9780470602638.ch3.